Evolution of pore-shape and its impact on pore conductivity during CO_2 injection in calcite: Single pore simulations and microfluidic experiments

Priyanka Agrawal [a,*], Amir Raoof [a], Oleg Iliev [b,c], Mariëtte Wolthers [a]

[a] Department of Earth Sciences, Utrecht University, Utrecht, the Netherlands
[b] Fraunhofer Institute for Industrial Mathematics ITWM, Kaiserslautern, Germany
[c] Institute of Mathematics and Informatics, Bulgarian Academy of Sciences, Sofia, Bulgaria

ARTICLE INFO

ABSTRACT

Injection of CO_2 into carbonate rocks causes dissolution and alters rock transport properties. The extent of the permeability increases, due to the increased pore volume and connectivity, strongly depends on the regimes of transport and dissolution reactions. Identification of these regimes and their parametrization at the microscopic scale is required for an understanding of the injection processes, and, afterward, for calculating the effective macroscopic parameters for field-scale simulations. Currently, a commonly used approach for calculating the rock effective parameters is the Pore Network Method, PNM, but a better understanding of the validity of its basic assumptions and their areas of applicability is essential. Here, we performed a combined microscopic experimental and numerical study to explore pore-shape evolution over a wide range of transport and dissolution reaction regimes. Experiments were conducted by flowing an acidic solution through a microscopic capillary channel in a calcite crystal at two different flow rates. The experimental results were used to validate our pore-scale reactive transport model that could reproduce the measured effluent composition as well as pore shape changes. Two key stages in pore shape evolution were observed, a transient phase and a quasi-steady-state phase. During the first stage, the shape of the single pore evolved very fast, depending on the flow regime. Under advective-dominant flow, the pore shape remained nearly cylindrical, while under diffusive-dominant transport, the pore shape developed into a half-hyperboloid shape. During the quasi-steady-state stage, the pore volume continued to increase, however, without or with diminutive change of the pore shape. In this stage, only a long period of injection may result in a significant deviation of the pore shape from its original cylinder shape, which is a common assumption in PNMs. Furthermore, we quantitatively evaluated the impact of evolved pore shape spectrum on the conductance calculations and compared it to the formulations currently used for pore network modeling of reactive transport. Under low flow rates, neglecting the developed non-uniform pore shape during the non-steady stage may lead to an overestimation of pore conductance up to 80%.

1. Introduction

Geological sequestration of CO_2 in carbonate reservoirs is considered to be a promising solution for mitigating the global warming problem caused by greenhouse gas emission (Hawez and Ahmed, 2014; Liao et al., 2012; Pacala and Socolow, 2004; Shaw and Bachu, 2002). Injection of CO_2 into such rocks triggers a series of chemical reactions, most importantly calcite dissolution, that may cause changes in pore shape, connectivity, and tortuosity (e.g., Rathnaweera et al., 2016). Accurate predictions of these changes are important in order to control the injection rate and to assess the long-term stability of the stored CO_2 (Rochelle et al., 2004).

Traditionally, the dissolution of carbonate rocks by acidic, CO_2-rich, solutions is simulated at the Darcy scale, which solves macroscopic equations over averaged porous media with the assumption that each spatial element of a porous medium is a well-mixed volume. However, the fluid transport processes and geochemical reactions occur at the pore-scale of the reservoir rock, where the solid-fluid interface are well defined. Therefore, confident prediction of rock transport properties from continuum scale models needs input from pore-scale models. Several research groups have utilized 3D micro-CT images or virtually generated geometries to simulate the coupled physical and chemical processes at the pore-scale, however, they are limited to a relatively small amount of pore volumes even with the existing computational power.

Another powerful approach to investigate these coupled subsurface processes at the pore scale is Pore Network Modeling (PNM) where the pore space is represented by a set of pre-defined shapes for pore

---

bodies and throats. PNMs enable simulations on orders of magnitude larger rock volumes compared to the full 3D pore-scale simulations, due to a simplified representation of pore geometries. Several reactive PNMs, capable of handling evolving geometries, have been proposed in the literature in the context of CO_2 related problems (Algive et al., 2010; Mehmani et al., 2012; Nogues et al., 2013; Raoof et al., 2012; Tansey and Balhoff, 2016; Varloteaux et al., 2013b, 2013a). For instance, microscopic pore wall evolution can be related to the change in porosity and permeability using dimensionless numbers (Algive et al., 2010; Varloteaux et al., 2013a, 2013b). In other available PNMs, the geometry modification assumes that pores open linearly, without changing shape, irrespective of reaction and transport regime (Mehmani et al., 2012; Nogues et al., 2013; Raoof et al., 2012). The validity of these assumptions can be tested using microfluidics experiments and detailed simulations at the single-pore scale.

Single-pore models, allow a detailed description of reactive transport processes (Chen et al., 2014a,b; Kang et al., 2003; Kumar et al., 2011; Li et al., 2008a,b; Van Noorden, 2009). These models simulated coupled processes in the context of carbonate dissolution for fixed geometry (Li et al., 2008) and relatively simple chemical system or evolving geometry (Chen et al., 2014a,b; Kang et al., 2003; Kumar et al., 2011; Li et al., 2008b; Van Noorden, 2009). Recently, Gray et al. (2018) investigated a single channel drilled through solid calcite and a pristine Ketton Oolite core plug. They observed that the cylindrical pore evolves into a nonlinear half-hyperboloid shape. However, they did not investigate the flow and reactive transport regimes under which the nonlinear pore shape developed, and the influence of different transport and reaction parameters on the developed pore shape.

Here, we combine microscopic experiments with numerical simulations at the single-pore scale to investigate the impact of acidic-solution injection on pore-shape evolution in calcite. We have used the Stokes equation for fluid flow coupled with solute advection-diffusion equations and multicomponent chemical reactions. The evolution of the explicitly defined calcite solid-fluid interface is simulated using arbitrary-Lagrangian Eulerian (ALE) method. The developed model is validated by microfluidic experiments conducted in single pores drilled through optical-grade calcite crystals. Confocal laser microscope was used to track the pore shape evolution. Furthermore, the chemical composition of the effluent solution was measured to validate the overall calcite dissolution rate. Depending on flow-regime, our results showed an initial intense pore-shape change while the concentration gradients turn into a quasi-steady state. Once quasi-steady state was attained, the continued dissolution lead to an additional pore widening, with limited change of pore shape over time, which deviates from the original cylinder shape only for long periods of injection We have quantitatively evaluated the impact of our results on assumptions relating conductance evolution for PNM models that assume a linear pore opening. The goals of this paper are as follows:

(i) To validate the numerically simulated pore shapes against the microfluidic lab experiments.
(ii) To perform a systematic study of different flow, transport and reaction conditions in order to identify the regimes for which the currently used PNMs are providing reliable results and the regimes for which the usage of PNMs assuming constant cylindrical pore shapes can lead to significant errors.
(iii) To calculate the pore conductance through the direct simulation algorithm presented here as well as using state of the art approaches used by PNMs, and compare the two methods.

2. Materials and methods

2.1. Single pore simulations

To simulate pore evolutions, fluid flow and multi-complement transport processes were solved fully coupled with moving boundaries due to

dissolution reactions (SI, Section S1). A Finite Element method was used (COMSOL Multiphysics®) and a Backward-Euler time stepping method was implemented for time discretization.

2.1.1. Fluid flow and transport

In this study we have considered slow fluid velocity only (i.e., Reynolds number $Re << 1$). Therefore, the inertial terms can be neglected in the momentum equations and the Stokes equation may be used to compute the velocity field and the pressure in the single pore:

$$\rho \frac{\partial u}{\partial t} + \nabla.p = \mu \Delta u \tag{1}$$

$$\nabla.u = 0 \tag{2}$$

where, p is pressure, ρ is the fluid density and μ is the fluid viscosity. The density and dynamic viscosity of water were 998.25 kg m^{-3} and 8.96×10^{-4} Pa s, respectively. The concentration of the dissolved species is assumed to be low enough so that the fluid density and the viscosity changes are negligible. At the inlet, a constant mass flux condition is imposed, and a constant pressure of 1.0 bar is applied at the outlet. At the lateral boundaries of the pore, no-slip boundary conditions are imposed. The normal velocity at the lateral pore boundaries is continuous, i.e., the normal fluid velocity at the interface is equal to the normal velocity with which the solid wall moves due to the solid surface dissolution.

Initialy, i.e., at time zero, it is assumed that the pore with calcite walls is in equilibrium with the steady-state flow. The simulation starts by dropping the pH of the injecting fluid via the inlet of the pore, which initiates the dissolution process leading to pore geometry evolution. During the simulation, the velocity field is updated to account for the pore geometry changes.

To simulate the transport of each dissolved species, advection-diffusion-reaction equation is implemented:

$$\frac{\partial c_i}{\partial t} + \nabla.(-D_i.\nabla c_i) + \nabla.(u.c_i) = R_i \tag{3}$$

where, D_i, c_i and R_i are diffusion coeffcient (m^2 s^{-1}), concentration (mol m^{-3}) and reaction input of species i^{th} (mol m^{-3} s^{-1}), respectively.

At the pore inlet we implemented a flux-based boundary condition (Starchenko et al., 2016). This flux depends upon the fluid velocity and the concentration values specified.

$$n.(-D_i.\nabla c_i + u.c_i) = u_n.c_{oi} \tag{4}$$

where, c_{oi} is the inlet (injected) concentration of species ith and u_n is the normal velocity at the inlet. The concentration for each aqueous species is given in Table 1. The outlet boundary is exposed to zero gradient condition for all species. To conserve the mass across the solid-fluid interface, the total (diffusive plus convective) flux for species involved in the surface reactions. i.e., Ca^{2+} and CO$_3$$^{2-}$ equals the reactive flux at the interface. This reads:

$$-n.(-D_i.\nabla c_i + u.c_i) = R_{Calcite} \tag{5}$$

where, $R_{Calcite}$ [mol m^{-2} s^1] is the surface reaction rate as discussed in SI, Section S1.1.

2.1.2. Geochemical model

The injected solution into the carbonate rock reservoirs contains dissolved CO_2. This leads to the formation of the weak carbonic acid and its dissociation to establish new equilibria with HCO$_3$$^-$ and CO$_3$$^{2-}$ species. The reactions involving the dissolution of CO_2 in the water are much faster than any other fluid-mineral reactions (Rochelle et al., 2004), as long as the pH < 9 (Wolthers et al., 2008; Zeebe and Wolf-Gladrow, 2001) which is the situation for this study. Therefore, we can safely assume that solution-phase reactions are of equilibrium type (SI, Section S1.1). Calcite dissolution occurs at the fluid-solid interface which is represented by the lateral boundaries of the pore. The dissolution rate laws applied at these boundaries are based on the study

Table 1

Concentrations and self-diffusion coeffcients of aqueous species in the injecting solution and in the initial solution inside pore.

Species	Injecting solution – I (mol m^{-3})	Injecting solution – 2 (mol m^{-3})	Injecting solution – 3 (mol m^{-3})	Injecting solution – 4 (Solution corresponding to the experiment) (mol m^{-3})	Initial solution inside pore (mol m^{-3})	Diffusion coeffecient (m^2 s^{-1}) [a]from Li and Gregory, 1974 and [b]from Liu et al., 2011
H$^+$	1.1	5.02×10^{-1}	1.63×10^{-1}	1.26×10^1	1.27×10^{-7}	[a]9.31×10^{-9}
OH$^-$	1.58×10^{-8}	3.54×10^{-8}	1.09×10^{-7}	1.43×10^{-9}	8.35×10^{-2}	[a]5.27×10^{-9}
CO$_2$(aq)	1.51×10^3	3.07×10^2	3.23×10^1	1.07×10^{-2}	2.27×10^{-5}	[a]1.19×10^{-9}
HCO$_3^-$	1.04	4.74×10^{-1}	1.54×10^{-1}	6.7×10^{-7}	8.35×10^{-2}	[a]1.19×10^{-9}
CO$_3^{2-}$	1.34×10^{-7}	1.34×10^{-7}	1.34×10^{-7}	7.68×10^{-15}	3.38×10^{-2}	[a]0.92×10^{-9}
Ca^{2+}	0	0	0	0	0.12	[a]0.79×10^{-9}
Na$^+$	2.00×10^2	2.00×10^2	2.00×10^2	2.00×10^2	0	[b]1.34×10^{-9}
Cl$^-$	2.00×10^2	2.00×10^2	2.00×10^2	2.13×10^2	0	[b]1.86×10^{-9}
pH	3.1	3.4	3.9	2	9.91	–
pCO$_2$	100	10	1	3.31×10^{-4}	6.76×10^{-7}	–

by Busenberg and Plummer (1986) (SI, Sections S1.1 and S3.1). Under acidic conditions, the overall dissolution rate strongly depends upon the activity of H$^+$ which becomes pH independent when values of pH are above 7. To calculate the activity coefficient of charged species, the Davies equation was applied.

2.1.3. Pore shape evolution model

Calcite dissolution results in a moving fluid-solid interface problem. For such problems, the arbitrary Lagrangian–Eulerian (ALE) method is considered to be very precise as the solid-fluid boundary can be exactly tracked (Kumar et al., 2011; Soulaine et al., 2017; Van Noorden, 2009). (see Kumar et al., 2013 for more details on the ALE method in the context of reactive transport related problems).

A displacement rate, normal to the pore surface, is assigned to the reactive walls which depend on the amount of the dissolved calcite, and thus on the reaction rate of calcite dissolution. We should note that in the free boundary problem considered here, the displacement rate of the pore wall (i.e., the solid-fluid interface) is not a predefined constant value or function, instead, it is calculated at each time step and for each point along the pore length (SI, Section S1.2). This makes the dissolution rate a dynamic nonlinear parameter which depends on the solution composition.

2.1.4. Physical-chemical parameters

The initial cylindrical pore geometry is representing a single pore located in a carbonate rock sample. For model validation, the dimension of the pore was set using the size of the capillary tube used in experiments, being length, $L = 2 \times 10^{-3}$ m, and, radius $r = 2.5 \times 10^{-4}$ m. For models used for analysis, the dimension of the pore was set equal to the naturally occurring pore sizes i.e., $L = 5 \times 10^{-4}$ m, and, $r = 4 \times 10^{-5}$ m.

The pore is initially filled with calcite-saturated water. The equilibrium concentration of species corresponding to this condition is listed in Table 1. Unless specified otherwise, the diffusion coefficients for all species were assumed identical, with a value of 3.36×10^{-9} m^2 s^{-1} which is the average of the self-diffusion coefficient of species present in the reactive system (as listed in Table 1, hereafter this model is referred as Model I).

We performed several simulations by applying different flow velocities to cover a range of transport regimes, from diffusion dominated to advection dominated conditions. Moreover, by changing the chemical composition of the injecting solution we aimed to explore the impact of different reaction regimes. For the model validation, two flow rates corresponding to the microfluidic experiments were implemented which were equal to 8.3×10^{-11} and 8.3×10^{-10} m^3 s^{-1}, resulting in an average velocity of 4×10^{-4} and 4×10^{-3} m s^{-1}, respectively. For the further analysis of the single pore system, five flow rates were imposed in our model, including 2×10^{-10}, 2×10^{-11}, 2×10^{-12}, 2×10^{-13}, 2×10^{-14} m^3 s^{-1}. This resulted in average velocity values of 4×10^{-2}, 4×10^{-3}, 4×10^{-4}, 4×10^{-5} and 4×10^{-6} m s^{-1}.

The injected solution is in equilibrium with a certain pCO$_2$ value (pressure of CO$_2$ gas). The concentration of all species with the target pCO$_2$ values were obtained using PHREEQC (Parkhurst and Appelo, 2013) with the phreeqc.dat database. In this study, pCO$_2$ values of 100.0, 10.0 and 1.0 bar were chosen to represent different reaction regimes. The corresponding values of the species concentrations in these solutions are listed in Table 1. To implement the experimental conditions as accurately as possible in the COMSOL model, the injecting solution composition was matched to the pH 2 using HCl acid in place of pCO$_2$. The details of this solution are given in Table 1.

2.1.5. Parametrization of the flow and reaction regimes

In order to analyze the relative strength of advection, diffusion, and reaction, we use dimensionless Péclet number and Damkhöler number. The Péclet number, Pe, compares the characteristic times of diffusion and advection transport processes as:

$$Pe = \frac{vr}{D} \tag{6}$$

where v is the average velocity at the inlet boundary and r is the radius of the channel at the inlet. Due to the dissolution, the radius at the inlet changes, and this leads also to the change of the inlet velocity. Both effects indicate that Pe and Da change with time.

The Damkhöler number, Da, measures the solution reactivity compared to the advection rate as:

$$Da = \frac{T_A}{T_R} \tag{7}$$

$$T_A = \frac{r}{v} \tag{8}$$

$$T_R = \frac{C_{Calcite}}{S_R} \tag{9}$$

T_A and T_R are the advection time scale and reaction time scale, respectively. S_R is the surface reaction rate, noted at the end of the first stage from the inlet pore wall (mol m^{-2} s^{-1}) and $C_{Calcite}$ is the density of surface sites of calcite at the start of dissolution (mol m^{-2}). This is calculated from the surface site density data i.e., 4.9 calcite molecules per nm^2 based on crystallographic data for the dominant cleavage plane of calcite (e.g., Wolthers et al., 2008) and Avogadro number (6.023×10^{23}), providing $C_{Calcite}$ as 0.8×10^{-5} mol m^{-2}.

As Pe and Da numbers change over time, we examine the results with respect to the initial Pe and Da numbers calculated at the inlet boundary of the pore. Table 2 provides the Da and Pe numbers corresponding to the numerical simulations (Model-I), where simulations 1 and 2 were used for the model validation and simulations 3–11 were used for the pore shape analysis.

2.2. Microfluidic experiments

To directly observe pore evolution and to validate our numerical model, microfluidic experiments were conducted using a channel of

Table 2
Simulations using different flow rates and reaction parameters to cover a range of *Da* and *Pe* numbers.

Simulation no.	pH of the injecting solution	Average velocity (m s^{-1})	*Pe*	*Da*
1	2	4×10^{-3}	314.64	3.96
2	2	4×10^{-4}	31.46	27.40
3	3.1	4×10^{-3}	47.4	0.96
4	3.4	4×10^{-3}	47.4	0.21
5	3.9	4×10^{-3}	47.4	0.03
6	3.1	4×10^{-4}	4.74	9.1
7	3.4	4×10^{-4}	4.74	1.98
8	3.9	4×10^{-4}	4.74	0.29
9	3.4	4×10^{-5}	0.47	14.95
10	3.9	4×10^{-5}	0.47	2.13
11	3.9	4×10^{-6}	0.05	5.5

radius 2.5×10^{-4} m and length 2×10^{-3} m, drilled in optical grade calcite crystal (Iceland spar). A laser fluorescence confocal microscopy (Nikon A1R confocal) was used to image the extent of dissolution and the pore shape change. For the fluorescent dye, fluorescein sodium salt (Lot No.: BCBM7214V; Sigma-Aldrich; emission wavelength – 515 nm) was used. The injection solutions were prepared using deionized water equilibrated with atmospheric CO_2 and adjusted to desired pH value of 2 with 1 M stock solution of HCl acid. To ensure the sufficiently constant ionic activity of solutions, 0.2 M equivalent NaCl salt (Lot No.: K48328204648) was added. At the start of each experiment, $CaCO_3$ saturated water is injected in the channel, to attain the approximate carbonate reservoir initial conditions. The solutions were injected with the use of a syringe pump (11 Pico Plus Elite, Harvard Apparatus) and a 5 ml Gastight syringe (Hamilton 1700 series) at the desired flow rates.

Effluent measurements were done to obtain changes in pH and Ca^{2+} concentration due to the dissolution of the calcite. Orion micro pH electrode was used for the pH measurement of the effluent solution. Inductively coupled plasma-optical emission spectrometer (ICP-OES, SPECTRO ARCOS) with a cross flow Nebulizer, was used for the Ca^{2+} concentration measurement. The collected outflow samples for the period (0, T] were diluted with 2% HNO_3 solution to attain the minimum required sample volume of 6 ml for ICP-OES measurements. Measured Ca^{2+} concentration from the outflow solution is compared to the flux-weighted averaged concentration of Ca^{2+} at the pore outlet of the numerical model, calculated as:

$$cCa_{OUT} = \frac{\int_0^{r(T)} cCa(\acute{r})u(\acute{r})\,\acute{r}\,d\acute{r}}{\int_0^{r(T)} u(\acute{r})\,\acute{r}\,d\acute{r}} \tag{10}$$

here, $cCa(\acute{r})$ and $u(\acute{r})$ are the Ca^{2+} concentration and velocity, at the radial distance of $\acute{r}$, respectively. $r(T)$ stands for the outlet radius of the pore at time $t = T$. Radial symmetry of the solution is assumed, thus no integration with respect to the angle φ in the cylindrical coordinates is needed.

Displacement of the calcite surface was quantified with reference to the position of the inert glass section attached to the inlet face of the channel. Additional details of material and methods are provided in SI, Section S2.

The experiments were conducted at two flow rates with one order of magnitude difference (i.e., 5 μl min^{-1} and 50 μl min^{-1}) to inject the solution with a pH value of 2. These flow rates yielded average velocities of 4.2×10^{-4} m s^{-1} and 4.2×10^{-3} m s^{-1}, respectively.

3. Results and discussion

3.1. Validation of the numerical model outcome with experiment results

Fig. 1 shows the Ca^{2+} concentration and the pH at the outflow obtained by measurements and using the numerical simulations. The agreement between modeling and measured data was good for Ca outflow concentrations and reasonably well for pH under both flow rates.

The simulation results for pore shape evolutions also showed a good agreement with the experimentally observed pore shape under both flow regimes (Fig. 2). Under high flow rates, the channel evolved almost uniformly (with only minor curvatures of the pore wall near to the inlet) and almost retained the original cylindrical pore shape (Fig. 2a and c). Under low flow rate conditions, the channel evolved to a non-uniform half-hyperboloid shape, with a strong curvature developing close to the pore inlet (Fig. 2b and d). In the high flow rate experiment, average pore-wall displacement was calculated using the average of the top pore wall displacement and the bottom pore wall displacement. We found a similar value for the experiment (equal to 51 μm, shown in Fig. 2a) and simulations (equal to 61 μm, shown in Fig. 2c) after injecting the same number of pore volumes. In contrast, under low flow rate, the magnitude of experimentally observed average pore-wall displacement (with a value of 179 μm) was overestimated by the model which provide a value of 252 μm (Fig. 2b and d).

For high flow rate, both effluent measurement and microscope image-based results are within the experimental error with the model utilizing a single diffusion coefficient for all aqueous species. Also, the agreement between the amount of dissolved calcite from the microscopic and the simulated image of the channel (Fig. 2) indicates that the reactive-transport model appropriately captures the dissolution rate (i.e., the pore evolution). In the low flow rate experiment, the disagreement between the obtained calcite surface displacement value using modeling and experiments is within the range of the uncertainty of the input parameters, i.e., reaction rate constants and the choice of diffusion model (details are provided in SI, Sections S3.1 and S3.2). We observed that the system remains far from the equilibrium for the whole duration of the experiment (Fig. S5) which supports the capability of the implemented rate model to capture the dissolution process throughout the experiment period.

We also found that changing the diffusion coefficients or using species-specific diffusion coefficients would not improve the results. Therefore, as pore shape evolution under varying fluid velocity and composition is captured well by using a single diffusion coefficient model, we have applied Model I for further analysis.

3.2. Initial stages of pore shape development

The pore fluid is initially at equilibrium with calcite proving a pH value of 9.9. Injection of an acidic solution with a pH value of 3.9 and pCO$_2$ value of 1.0 bar, shifts the equilibrium conditions of the pore fluid, differently under different flow regimes. The injection initiates calcite dissolution through a set of bulk reactions as well as surface reaction. The surface reaction products, i.e., Ca^{2+} and CO_3^{2-}, accumulate within the boundary layer near the pore wall from where they move away towards the bulk fluid. The amount of reaction products strongly depends on the difference between pH of the injected solution and that of the initial pore fluid. We observe a front propagation behavior along the pore at the initial stage of the reaction. In the advection-dominated flow
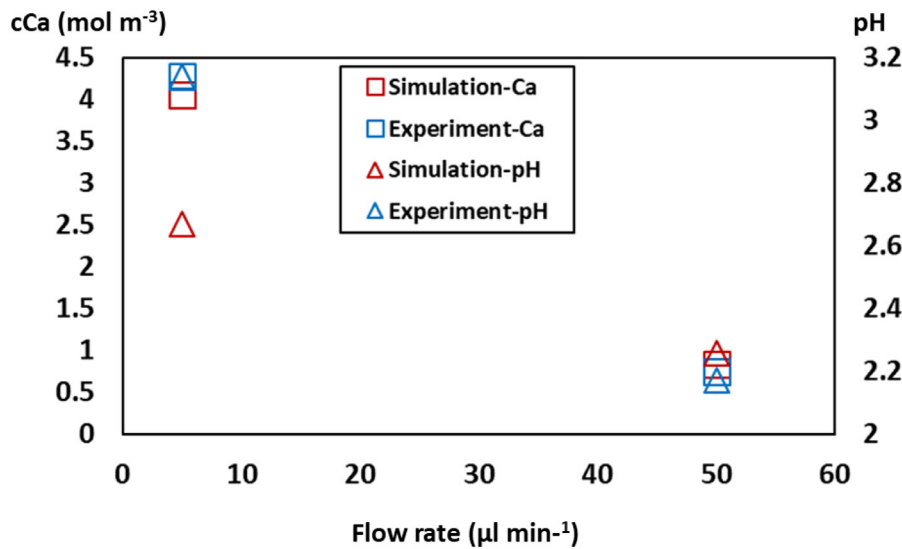
Fig. 1. Comparison of the measured Ca^{2+} and pH at the outlet of the experiment with the flux-weighted average concentration of Ca^{2+} and pH from the numerical simulations (Model-I). The error on the Ca and pH measurements is the same as the symbol size.
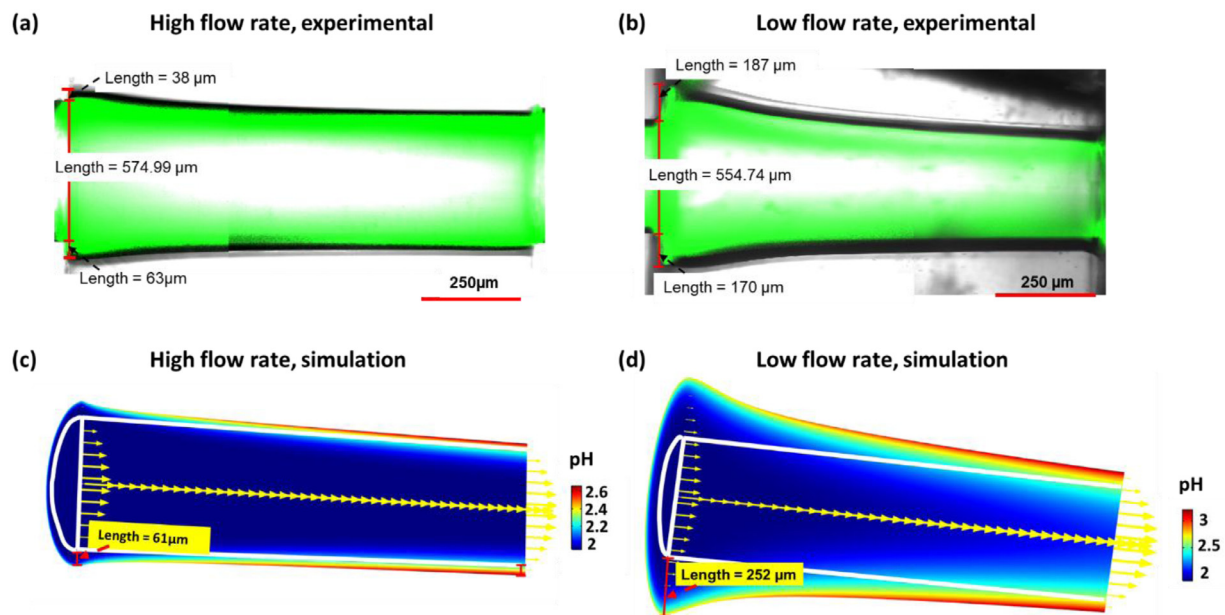

Fig. 2. Comparison of high flow rate (50 μl/min corresponding to $Pe = 314.64$, Da = 3.96) and low flow rate (5 μl/min corresponding to $Pe = 31.46$, Da = 27.40) experimental observations with the numerical simulations. (a) and (c) show results under the high flow rate after injecting a solution of pH value of 2 for 3600 s, and (b) and (d) show results under the low flow rate after injecting a solution of pH value of 2 for 36,000 s. Images in a and b plots were acquired by superimposing images from the transmitted detector and the fluorescein detector (Figs. S2 and S3). Simulation results are for the same flow rate and fluid composition and a similar number of pore volumes, with colours showing solution pH within the channel and, arrows indicating the velocity field. Arrow length is proportional to velocity. The inner white cylinder indicates the initial channel shape (i.e., at $t = 0$ s); the coloured regions located outside the cylinder indicate dissolved parts during the reaction.

regime ($Pe>1$), the Ca^{2+} rich zone, that is initially near the pore wall at the pore inlet (Fig. 3a, plot a), is predominantly transported downstream along the pore wall (Fig. 3a, plots b and c) before reaching the central part of the pore. As such, the longitudinal gradient smoothens faster than the transversal (i.e., cross-sectional) gradient, yielding concentration profiles with a prominent transversal gradient (Fig. 3a, plot d). Whereas in diffusion dominated flow regime ($Pe < 1$), the Ca^{2+} plume is shorter and more intensive (i.e., with a higher concentration of the reaction products) (Fig. 3b, plot a). The reason is that at $Pe = 0.47$, the flow velocity is slower, and more time is available to wash out the dissolution products. A stronger diffusive flux drives the transversal mixing as well, resulting in a concentration profile with a less prominent transversal gradient compared to the longitudinal gradient (Fig. 3b, plots b–d).

Although the low and high flow rate conditions lead to distinct concentration gradients, in both cases during the injection we observe two stages in the development of the concentration gradients. In the first stage, the concentration field changes significantly, leading to the establishment of a flow regime specific concentration field. Whereas in the second stage, referred to here as the quasi-steady stage, these changes become minute and the concentration gradients change only slowly. The quasi-steady state concentration gradient govern the dissolution and thus the pore wall evolution during the time. In the case when the concentration gradient along the wall is almost zero, the pore just expands in the normal direction without significant change of shape. In the case when there is a positive concentration gradient along the pore wall, the pore widens faster near the inlet compared to the outlet.
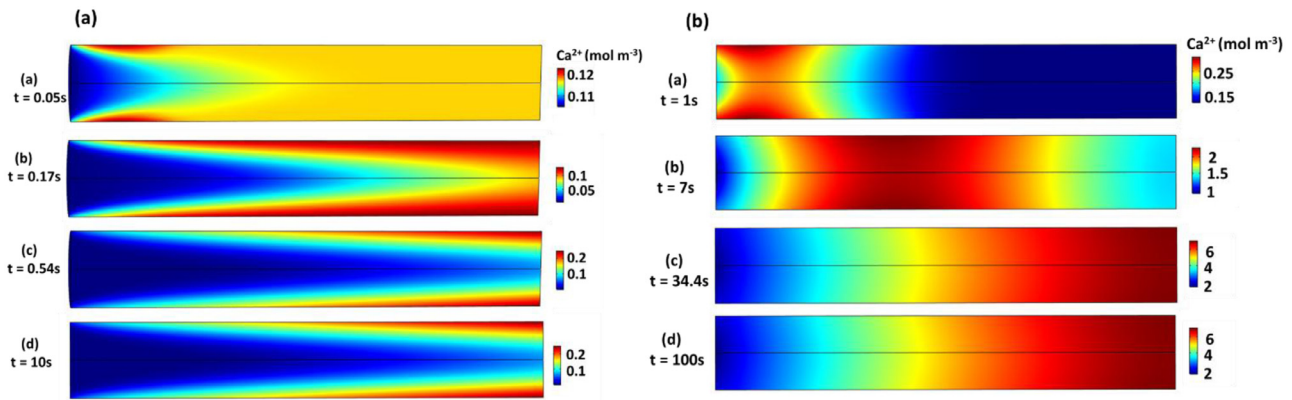
Fig. 3. Concentration field of Ca^{2+} over time inside pore space under flow rates corresponding to (a) *Pe* = 47.4 (b) *Pe* = 0.47. To improve the visualization of the concentration gradient, different scales have been used for all panels.
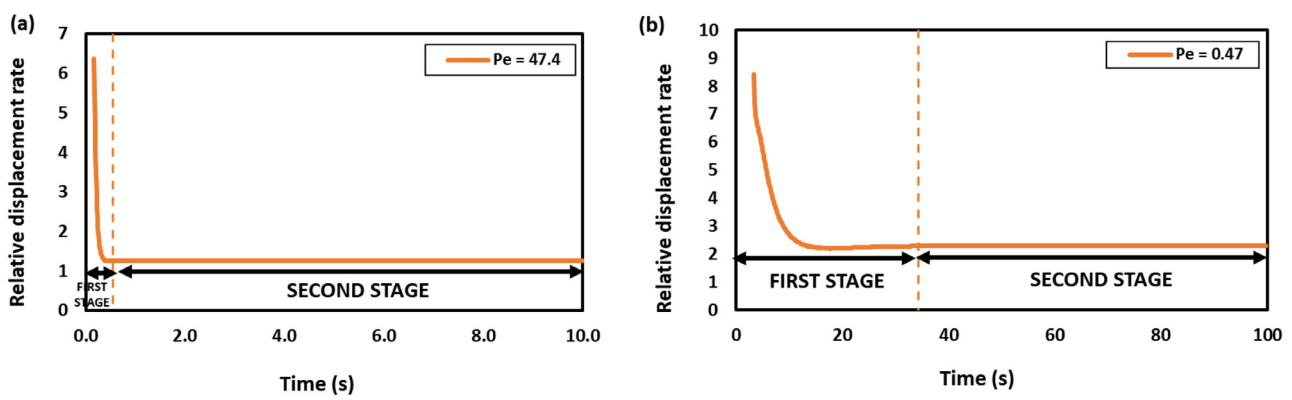

Fig. 4. Relative displacement profiles of the pore wall inlet compared to the pore wall outlet for the *Pe* numbers of (a) 47.4 and (b) 0.47. Note that the start of these plots is from the time when pore outlet point has displaced at least 0.01 nm. The marking of the end of the first stage, as indicated by the dashed vertical line, is at the time when the change in the relative displacement rate with time is less than 0.01% and the changes into concentration gradients becomes minute i.e., *t* = 0.54 for *Pe* = 47.4 and *t* = 34.4 s for *Pe* = 0.47.

To quantify the pore shape evolution during these stages and to explicitly mark the duration of the first stage, the relative displacement rate of the pore wall was calculated as the ratio of the displacement rate of the pore inlet to the pore outlet. At any time, the value of the relative displacement rate indicates how faster the pore inlet is displaced compared to the pore outlet. For example, for *Pe* number 0.47, initially inlet displacement rate is 8.5 times faster than the outlet displacement rate (Fig. 4b). During the first stage, the displacement rate of the pore outlet decreases constantly, and at the end of this stage, the relative displacement rate reaches an asymptotic value of 2.3 (Fig. 4b). Contrastingly, in the first stage for *Pe* number 47.4, this rate attains an almost constant value of 1.27 (Fig. 4a). Such evolution of the relative displacement rate of the pore wall results into a rigorous modification of the pore wall shape. The continuous change in the relative displacement rate is related to the shape of the pore at that time (shown in Figs. S7 and S8 for the example case of *Pe* number 47.4 and 0.47, respectively).

In conclusion, during the first stage, the concentration field modifies intensively, resulting into the intensive evolution of the pore geometry and the end of this stage is marked by a nearly established concentration gradients along the pore wall, providing a basis to find a predictive rate for the pore shape evolution.

While the pore shape evolves during the first stage, the pressure gradient remains constant (less than 0.1%, see SI, Section S3.3). This is due to the fact that the magnitude of the pore wall displacement in the short duration of the first stage is negligible compared to the overall aperture of the pore. Therefore, in the context of the simulated dissolution regimes and the pore dimensions, the geometry changes during the first stage of the dissolution can be neglected, which is in agreement with the theoretical evaluation of reactive transport regimes (Algive et al., 2010).

3.3. Evolution of the pore shapes under extended injection times

Although during the first stage the overall pore size would not increase considerably, the developed half-hyperboloid pore shapes indicate the dissolution pattern. The persisting longitudinal gradients in this stage imply that the pore inlet has a higher dissolution rate compared to the pore outlet.

The overall pore opening takes place during the second stage. To explain the pore evolution, we choose the simulation corresponding to the *Pe* number of 0.47 and *Da* number of 2.13. As concentration gradients are established along the pore after the first stage and considering that the reaction rate depends on the concentration gradients, dissolution of the interface at the inlet and at the outlet will take place at different speeds, however, with a predictive manner (Fig. 5). A remarkable observation was that for about 2,000,000 s (nearly 23 days), the reaction rate showed larger values at the inlet compared to the outlet. As a result, during this period the pore widened faster at the inlet compared to the outlet, deviating to a greater extent from the initial cylindrical shape. Initially, the calcite near the inlet dissolves about twice faster than close to the outlet (see also Fig. 4b), while at time scales well beyond 23 days we observe lower, however similar, dissolution rates at both inlet and the outlet faces (Fig. 5).
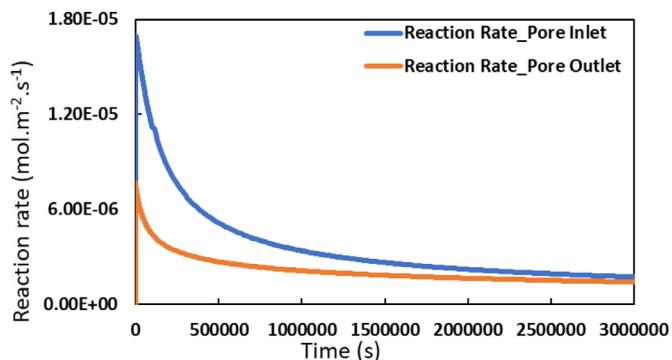
Fig. 5. Evolution of the reaction rate at the pore inlet and at the pore outlet for the half-hyperboloid shaped pore ($Pe = 0.47$, $Da = 2.13$).

Fig. 6 shows relative displacement rates modifying the pore shape during the second stage. The continued opening of the half-hyperboloid shape will eventually result in the development of a non-linear pressure profile. Fig. 6 shows the shape of the pore at two different times. At the time of 1000s, when the inlet radius has increased with about 1.5% (40.6 vs 40) and the outlet radius has increased 0.67% (40.3 vs 40), the pressure along the pore remains linear, meaning that at each point along the pore, we have a constant pressure gradient (recall, that the constant pressure gradient along a pore is an essential assumption in pore network algorithms). However, at $t = 30,000$ s, the pore shape develops so that the inlet radius has increased by 44% and the outlet radius by 18%, resulting in a non-linear pressure profile along the pore. In contrast, for $Pe = 47$, the relative displacement rate at the end of the first stage is close to one and the initially-cylindrical pore remains nearly cylindrical throughout the second stage and the pressure profile stays linear (Fig. S10).
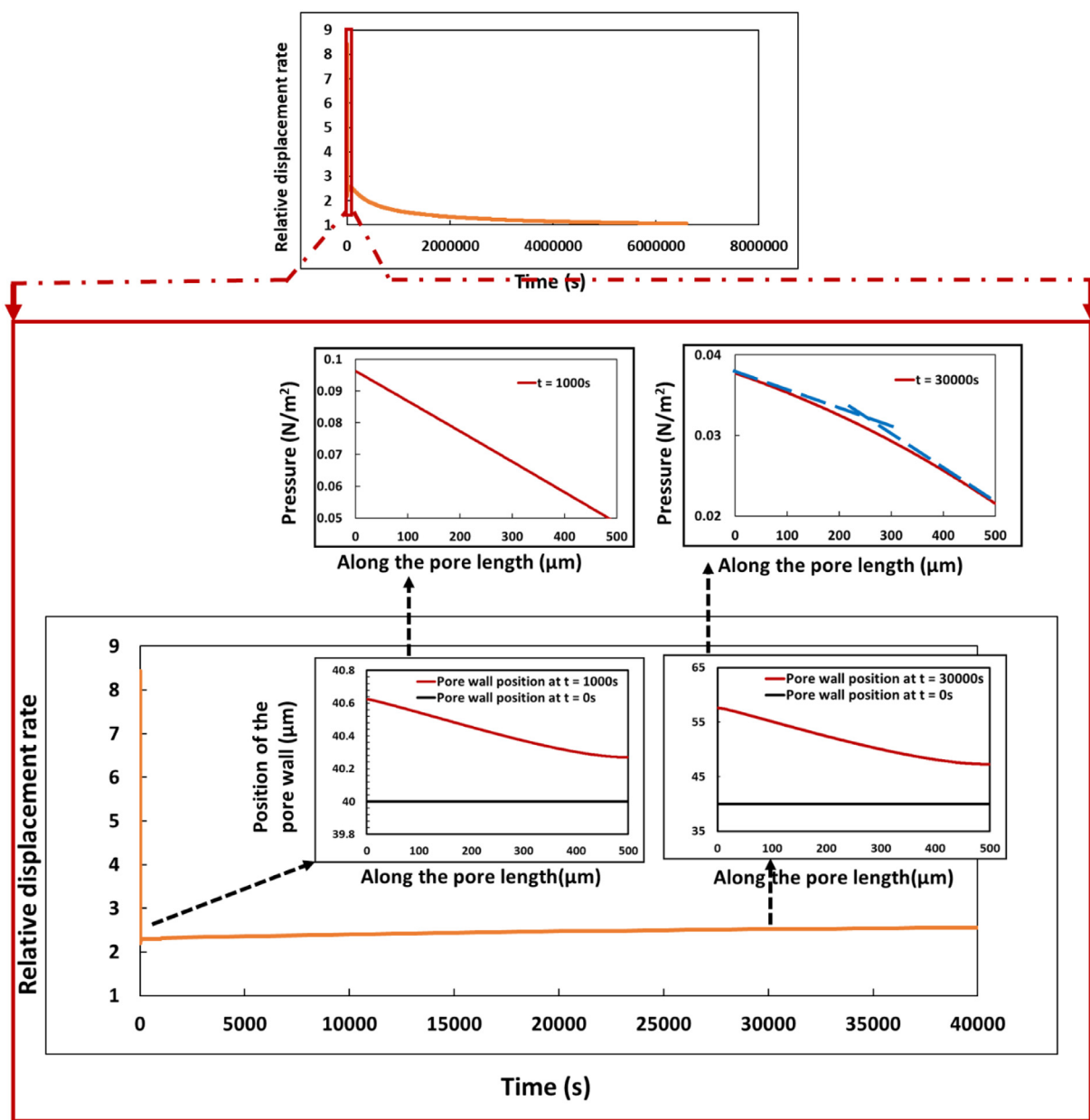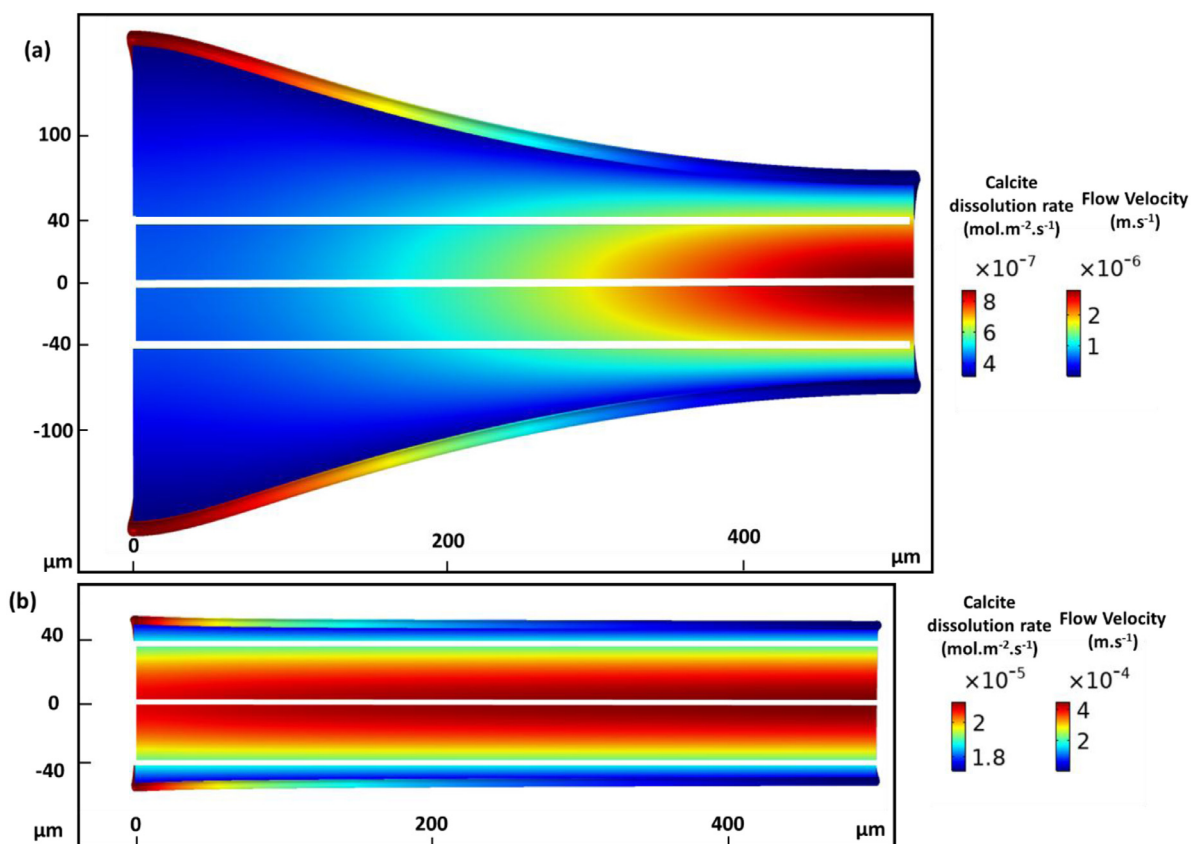

Fig. 6. Evolution of the relative displacement rate during the second stage for the case when at the end of the first stage, the pore shape is hyperboloid ($Pe = 0.47$, $Da = 2.13$). The evolved pore shapes and corresponding pressure profiles are shown in inset images, at $t = 1000$s, and 30,000 s. Note the different vertical axis scales in each inset image.

Fig. 7. Simulation results showing the evolved pore shape and the distribution of the velocity field and the reaction rate for two flow regimes of (a) $Pe = 0.05$ (b) $Pe = 4.74$. The injection period is 15,900 pore volumes for both cases with a pH value of 3.9 and pCO_2 value of 1.0 bar. The white lines indicate the initial pore shape and the coloured region outside of them indicates the dissolved zones during the reaction. The coloured rim at the pore wall shows the local calcite dissolution rates.

3.4. Flow rate effects on the pore shape evolution

To further explore the flow rate effects, we have performed several simulations by varying the Pe number while the pH of the inflowing solution was kept constant at a value of 3.9. At $Pe < 1$, the reaction products effectively diffuse into the pore bulk fluid region before any substantial longitudinal transport takes place (Fig. 3b). Near the inlet, strong diffusion of the reaction products toward the central parts of the pore facilitates calcite dissolution. At the same time, along the pore, the saturation index of the pore fluid with respect to calcite increases towards equilibrium, due to the buffering by the dissolution products, and dissolution rates decrease along the flow path. Consequently, dissolution reactions take place mainly close to the pore inlet, resulting in non-uniform pore widening and formation of a half hyperboloid-shaped pore (Figs. 2b and 7a). For $Pe > 1$, the transport is dominated by advection. Under this regime, the fast entering solution into the channel replaces the resident solution before the diffusion of the reaction products smoothens transversal gradients and buffers the pH of the solution. Therefore, the calcite pore wall is exposed to a reactive solution along the entire pore, resulting in an even dissolution rate and a nearly uniform evolution of the pore shape (Figs. 2a and 7b). Note that, at both flow rates, flow velocity increases towards the outlet face of the pore which reflects the constricted shape of the pore (Fig. 7).

Besides a difference in the shape evolution (i.e., a localized difference in calcite dissolution rate), there is also a clear difference in the total amount of dissolved calcite per injected pore volume. The simulation under low flow rate resulted in a higher value of calcite surface displacement per pore volume injected, compared to the simulation under a fast flow rate. This is because the solution residence time is larger

for the low flow rate simulation, and, therefore, reactants dissolve more calcite. However, when using time rather than injected pore volume, the low flow rate dissolves less calcite compare to a high flow rate over time. The evolution of the pore shape corresponding to all of the simulated flow rates is discussed in Section S3.4.

3.5. Chemistry effects on the pore shape evolution

In addition to the flow rate, the chemistry of the injecting fluid affects the pore shape. To explore chemistry effects further, we performed simulations with two injecting solutions at pH values of 3.1 and 3.9, corresponding to pCO_2 of 100.0 bar and 1.0 bar, respectively. Evolution of the pore shape depends on the reactivity of the pore wall towards the injecting solution. Expectedly, the pH = 3.1 solution results in the stronger displacement of the pore wall than the pH = 3.9 solution. This results in increased concentrations of the reaction products near the pore wall, driving the local solution chemistry towards equilibrium with respect to calcite. This buffering of fluid is also reflected by a change of the fluid pH, in the case of the pH = 3.1 inflow solution at $Pe = 4.74$, the transversal average pH increases from 4.71 to 4.82 corresponding to the dissolution rate from 1.70×10^{-4} [mol m^2 s^{-1}] to 0.49×10^{-4} [mol m^2 s^{-1}] from inlet to outlet boundaries, respectively. The result of this alteration in the pore fluid chemistry is ultimately reflected by the evolved pore shape. In this case, the pore widens non-uniformly along the pore length (Fig. S12a). However, injecting a pH = 3.9 solution at $Pe = 4.74$ provides a transversal average pH that changes from 4.09 to 5.10 and dissolution rate from 2.12×10^{-5} [mol m^2 s^{-1}] to 1.72×10^{-5} [mol m^2 s^{-1}], from the inlet to outlet boundaries, respectively. In this
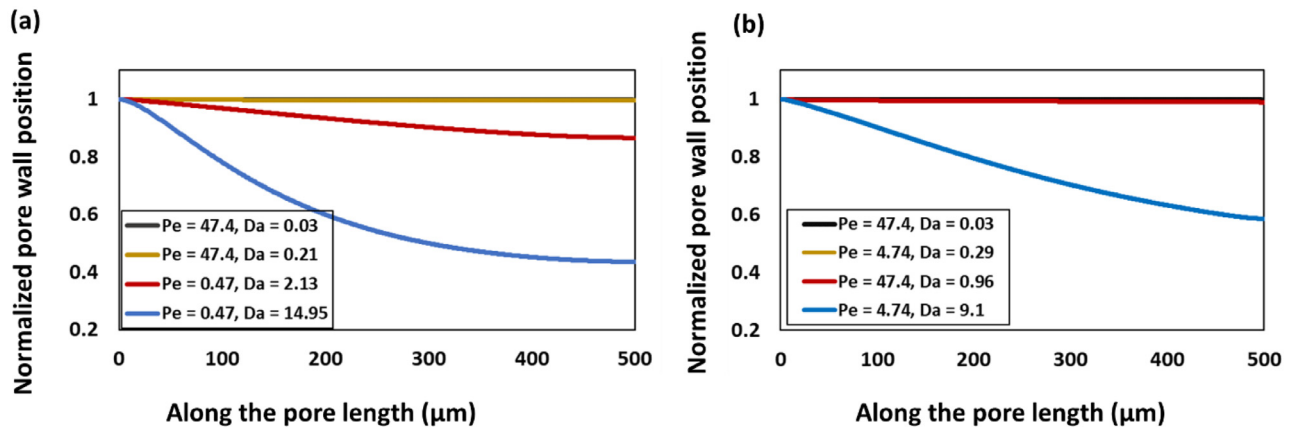
Fig. 8. The normalized position of the reacting pore wall under different reaction and flow regimes denoted by *Da* and *Pe* numbers respectively. In all cases, 1590 pore volumes were injected. (a) The pH of the injecting solution, reflected by high *Da* (see Table 2), impacts the pore shape more prominently for simulations with low *Pe* number (b) Injection flow rate impacts the pore shape more prominently for simulations using more acidic solutions.

case, fluid buffering during dissolution is relatively weaker and a more uniform pore shape develops (Fig. S12b).

To cover a range of values for Damköhler numbers, i.e., reaction regimes, we have chosen a combination of flow rates and injecting fluid chemistries (Fig. 8). Table 2 provides details of these simulations. By increasing *Da* number, the reaction time scale decreases compared to the advection time scale and the system approaches being transport limited instead of surface-rate limited. The normalized displacement profiles after injecting 1590 pore volumes, provided in Fig. 8, show that there is a monotonic relation between pore shape and *Da*, under the considered reaction regimes.

For *Da* < 1 and *Pe* = 47.4, reaction time scale is higher than the advection time scale, and at the same time advection dominates the diffusion. In such advection-dominated transport regimes, the chemistry of the injecting fluid has less control on pore shape evolution and adjusting inflow pH from 3.4 to 3.9 has a negligible impact over the pore shape (Fig. 8a, *Da* numbers 0.03 and 0.21). Whereas in the *Da* > 1 and *Pe* = 0.47 regime, which is overall reaction-dominated while transport is diffusion-dominated, the same shift of inlet pH causes a profound change in pore shape (Fig. 8a, *Da* number 2.13 and 14.95).

The dissolution regime corresponding to *Da* < 1 and *Da* > 1, can also be obtained by changing the pH of the injecting fluid. If the pH = 3.9 solution is injected, i.e., *Da* < 1, the impact of changing flow rate is less prominent over the pore shape and the pore shape remains nearly uniform (Fig. 8b, *Da* = 0.03 *Pe* = 47.4 versus *Da* = 0.29, *Pe* = 4.74). For a regime of *Da* > 1 using a reactive fluid with pH = 3.1, a shift of *Pe* number causes a significant change of the pore shape (Fig. 8b, *Da* number 0.96 and 9.1).

In reaction-limited dissolution regimes (*Da* < 1), control of flow rate and reactive strength of the injecting fluid becomes marginal over the shape of the pore. The reason is that the time necessary for dissolution-reaction (i.e., generating the reaction products and consuming protons) may dominate rather than the fluid mixing scale when analyzing the fluid buffering state. And in these regimes, dissolution is spatially homogeneous leading to uniformly developed pore shapes. Whereas in transport-limited dissolution regimes (*Da* > 1), fluid mixing strength exerts control over the chemical gradient inside pore space. This leads to heterogeneous dissolution process in which both flow rate and chemistry of the injecting fluid govern the pore shape.

To summarize, we can conclude that both injection parameters such as flow rate and fluid chemistry impart control over the pore shape. Fig. 9 provides a spectrum of pore shapes based on changes in transport and reaction regimes shown by *Pe* and *Da* numbers. The marking of the regimes in this study aligns well with the previously reported pore-scale work specific to the calcite dissolution for e.g., Soulaine et al., 2017.
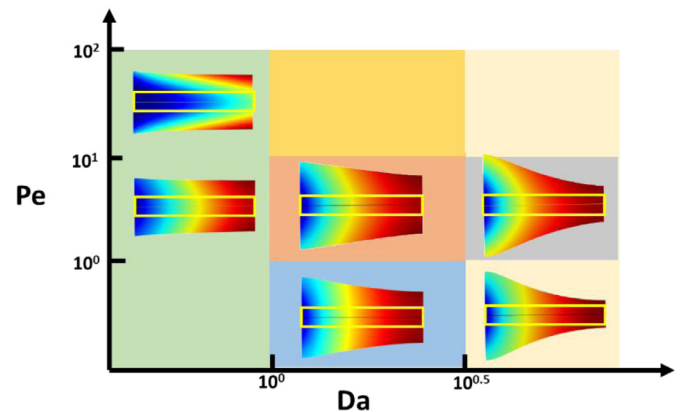

Fig. 9. Pore evolution after several hours of acid injection, based on changes in transport and reaction regimes shown by *Pe* and *Da*.

They have also observed the boundary between the uniform and non-uniform type of dissolution at *Da* number 1. In the subsequent section, we compare the conductance of a single pore after long injection period, calculated here with using fully coupled pore-scale model utilizing ALE method, and the approximate calculation of the conductance discussed in Pore Network algorithms, and investigate the related error depending on the dimensionless process parameters *Pe* and *Da*.

3.6. Implication of the pore shapes on the pore conductance

Evolution of conductance in dissolution simulations is implemented in existing pore network algorithms (e.g., Raoof et al., 2012, Mehmani et al., 2012, Raoof et al., 2013 and Nogues et al., 2013). A significant underlying assumption in this implementation is that the shape of the pore remains uniform, where the evolved pore shape still results in a linear pressure drop along the pore. The results presented here show that this assumption is valid under the advection-dominated flow regimes with *Pe* > 1 and transport-dominated reaction regimes with *Da* < 1. However, as we observed in the case of the *Pe* = 0.47, the changes of the shape start to influence the pressure profile in a time scale of 30,000 s which is within the time scale of injection period in a reservoir.

The pressure profile along a pore is directly related to the conductance calculated in PNM. Taking the commonly assumed laminar flow, when the pore changes are uniform along its length, the pressure drops linearly (Fig. S10). This is not the case when the pore shape deviates
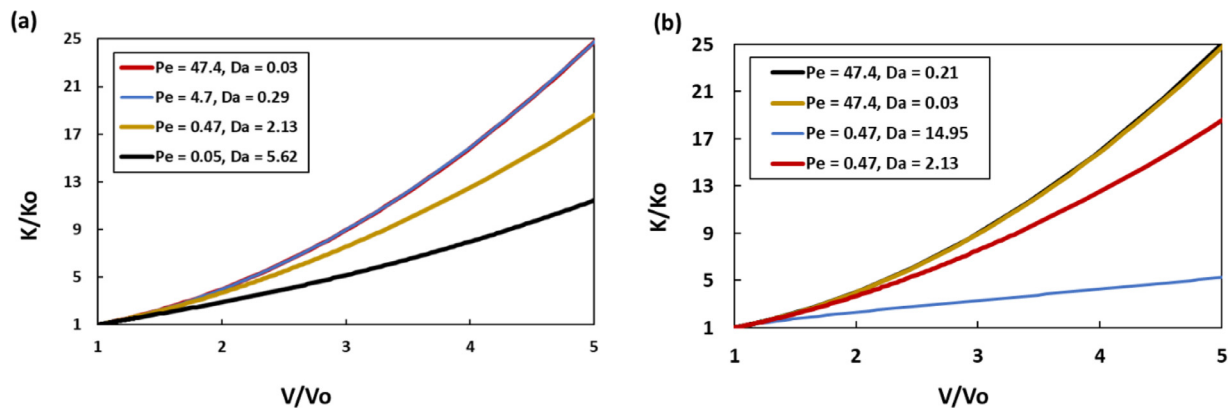
Fig. 10. Conductance of the pore as a function of pore volume for (a) different *Pe* numbers and constant fluid pH value of 3.9 (b) different *Da* numbers and two of the *Pe* number sets.

from the cylindrical one. In such a case the pressure gradient is not constant and changes along the pore (Fig. 6). Such pressure nonlinearity affects the pore conductance, and, therefore, the rock permeability. Hence, we need to quantify the impact of such modified shapes on the conductance of the pore.

The definition of conductance, *K*, is given via the flow rate, *Q* (m^3 s^{-1}) and the pressure drop ΔP (N m^{-2}) along the pore as:

$$Q = K\Delta P \qquad (11)$$

For a rounded cylindrical pore (with a constant diameter along the pore) with a parabolic velocity profile (i.e., Hagen - Poiseuille flow) the conductance, *K* (m^5 N^{-1} s^{-1}), is known and it is given by:

$$K = \frac{\pi(2r)^4}{128\mu L} \qquad (12)$$

here *L* is the length of the pore (called also pore throat length in the PNM literature) given in meters, (m), *r* is the radius of the pore (m). In dissolution experiments, as the radius $r = r(t)$ (and eventually, the shape of the pore changes), the pore conductance is no longer constant, $K = K(t)$. We calculated the apparent pore conductance (i.e., overall conductance of the pore) using Eq. (11). For Fig. 10, the conductance and pore volume is normalized with respect to the initial pore conductance and the initial pore volume, respectively.

The half-hyperboloid pore shape leads to a changing pressure gradient along the pore (Fig. 10a, black line). The narrowness of the pore aperture towards the outlet provides small contributions to the overall volume changes of the pore; however, this section of the pore controls the overall conductance of the pore. Consequently, pore volume increases considerably (near the pore inlet), while pore conductance changes marginally during hyperboloid pore shape formation (Fig. 10a, black line). This means that, as non-uniformity of the pore shape increases, the change of conductance becomes smaller for the same amount of volume change (Fig. 10). Therefore, at the pore scale, the change of the pore conductance in time in certain cases cannot be described just as a function of the pore volume, the pore shape may play a significant role. The implication of this observation for macroscale simulations is that formulae which provide permeability only as a function of porosity are not always suitable, and they are accurate only over a certain flow and reactive transport regime for which they have been developed.

In most of the existing pore network models, the conductance of the pore throat is updated at each time step in response to the changing volume of the pore only, without accounting for the pore shape evolution. And, such a conductance is obtained by utilizing either the volume of the connecting pore bodies (Nogues et al., 2013) or the volume of the pore throat (Raoof et al., 2012). We calculated the conductance of the simulated pore geometry in a similar method as used by Raoof et al., 2012.

At each time step, the volume of the pore provides the uniform radius of the pore which is further utilized in calculating the conductance. Fig. 11 shows the comparison of this conductance with the one calculated from the actual geometry of the pore, for two of the dissolution regimes.

We observe that if the dissolution process maintains the cylindrical shape of the pore, then the conductance is only a function of the volume of the pore, as assumed in PNMs (Fig.11b). Whereas, for the dissolution regime corresponding to $Pe < 1$ and $Da > 1$, the conductance of the pore does not remain a function only of the volume of the pore, but it depends also on the shape of the pore. In the latter case, ignoring the dependence of the conductance from the pore shape results in an error. The conductance calculated from the volume of the pore (PNM approach) overestimates by 38% the conductance calculated from the actual hyperboloid pore shape when the volume of the dissolved calcite is equal to the original volume of the pore. This overestimation is 76% when the volume of the dissolved calcite is equal to two times the original volume of the pore and may increase further with dissolution (Fig. 11a).

Note that the pore conductance evolution during the dissolution process depends not only on the flow and reaction regimes, as shown here (Fig. 10), but also on the length of the pore, on the initial radius of the pore, on the equilibrium pH and on the pH of the injected fluid. For the pH, radius and length of the pore investigated here, Fig. 12 summarizes the regimes in which the conductance can be calculated as in PNM only by the volume of the pore vs the regimes where this method fails to capture the correct conductance. This figure presents a moment during the dissolution process at which the change in the pore volume is 100% (i.e., V/V0 = 2). For the reaction-controlled regimes ($Da < 1$), irrespective of the flow rate, the volume-based conductance is within 1% range of the actual conductance. This difference increases significantly for the transport-controlled regimes, where the diffusion-dominated flow regimes yielding up to 76% of the difference. Note that the difference increases further with dissolving larger volume of the calcite. This result illustrates the limitation of the existing assumption in the pore network model, however, the work for deriving a more defined relationship for conductance remains a topic for future work. Although the presented insights about the pore-scale processes are based on a detailed geochemical model which includes both equilibrium and kinetic processes along with the multi-component solution system, it would be interesting future work to investigate the limitation of a simplified geochemical model against the current detailed model. Also, in this study we have presented two sets of microfluid experiments with an objective of validating the modeled pore shapes, however, utilizing such calcite micromodel setups to investigate the calcite dissolution processes under a wider range of transport and reaction regimes and in different pore geometries, remains future work.
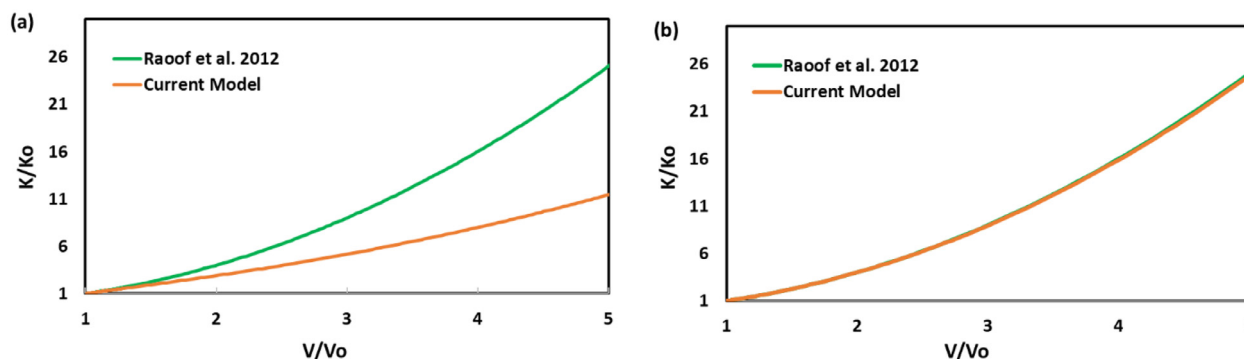
Fig. 11. Comparison of the pore conductance calculated from the actual shape of the pore vs an exemplary method from the existing pore network model for (a) *Pe* = 0.05 and *Da* = 5.62 (b) *Pe* = 47.4 and *Da* = 0.03.
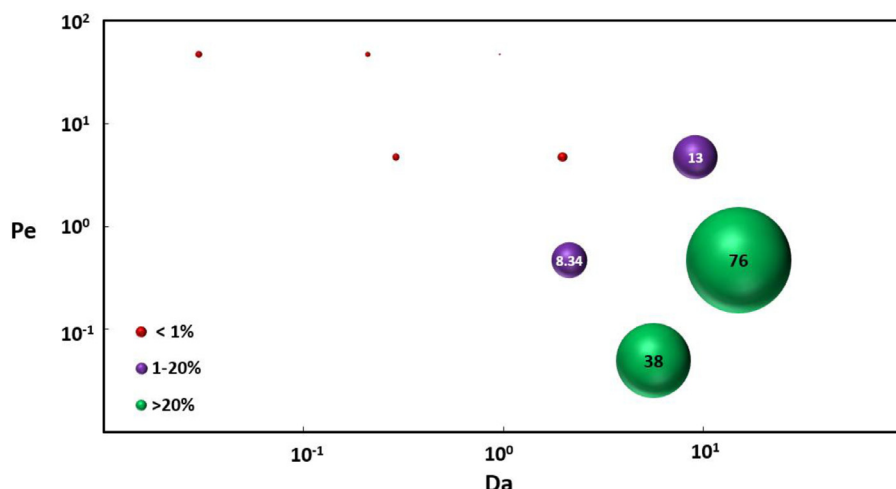

Fig. 12. *e-Da* phase diagram showing the% difference in the conductance based on the volume of the pore with the one from the actual pore geometry.

4. Conclusions

1. The simulation results of reactive transport processes through single calcite pore and the results from the respective microfluidic experiments were found to be in good agreement at both investigated flow rates. The validated computational algorithm was used to perform a thorough and detailed study of the dissolution processes for a range of hydrochemical parameters.

2. It was observed that the calcite dissolution process can be divided into two stages with respect to the concentration field development and pore shape evolution. During the first, very short (in the order of seconds) and intrinsically transient stage, the reactive-transport processes rapidly change the concentration field inside the pore, and at the end of this stage, the pore has attained a characteristic shape and concentration gradient. Only the latter plays a critical role in the longer-term dissolution process. These numerical results are a justification of the statements of other authors that the pore shape development during the first stage can be ignored, while the concentration gradient should be accurately calculated. The second stage is long (days or longer) and corresponds to real injection times in reservoirs. At this stage, the flow and transport are at a quasi-steady state. The pore shape changes slowly, but for large concentration gradients, significant deviation from the original cylindrical shape can be observed for certain dissolution regimes.

3. Generally, lower flow rates result in significant concentration gradients in the longitudinal direction and thus in a non-uniform change of the pore shape. As a result, the pressure gradient is no longer constant along the pore. An increase in solution reactivity (lowering in pH) provides the same effect; it drives reactions towards equilibrium

over a shorter distance from the inlet, and, therefore, results in non-uniform pore shapes. Injecting fluid with a high flow rate, or lower reactivity yields a more uniform pore volume increase. We also observe that the impact of flow rate and fluid reactivity on the pore shape are more significant when dissolution is transport controlled (*Da*>1).

4. For certain flow and reaction regimes, a significant difference is observed between the pore conductance computed here and pore conductance computed according to PNM (assuming constant pore shape). Further research is needed to understand if and how PNM can be used for dissolution regimes for which the basic PNM assumption leads to significant error in conductance evaluation.

Supporting information available

Additional details on numerical model and experiment methods and figures 1–12.

Declaration of Competing Interest

There are no conflicts to declare.

CRediT authorship contribution statement

Priyanka Agrawal: Conceptualization, Methodology, Formal analysis, Visualization, Writing - original draft, Writing - review & editing, Validation, Investigation. **Amir Raoof:** Conceptualization, Methodology, Formal analysis, Visualization, Writing - original draft, Writing - review & editing, Supervision. **Oleg Iliev:** Conceptualization, Methodology, Formal analysis, Visualization, Writing - original draft, Writing - review & editing, Supervision. **Mariëtte Wolthers:** Conceptualization,

Methodology, Formal analysis, Visualization, Writing - original draft, Writing - review & editing, Supervision, Funding acquisition, Resources, Project administration.

Supplementary materials

Supplementary material associated with this article can be found, in the online version, at doi:10.1016/j.advwatres.2019.103480.

References

Algive, L., Bekri, S., Vizika, O., 2010. Pore-Network Modeling dedicated to the determination of the petrophysical-property changes in the presence of reactive fluid. SPE J. 15, 618–633. https://doi.org/10.2118/124305-PA.

Busenberg, E., Plummer, L.N., 1986. A comparative study of the dissolution and crystal growth kinetics of Calcite and Aragonite. Stud. Diagenesis, U.S. Geol. Surv. Bull. 1578, 139–168.

Chen, L., Kang, Q., Carey, B., Tao, W.Q., 2014a. Pore-scale study of diffusion–reaction processes involving dissolution and precipitation using the lattice Boltzmann method. Int. J. Heat Mass Transf. 75, 483–496. https://doi.org/10.1016/j.ijheatmasstransfer.2014.03.074.

Chen, L., Kang, Q., Viswanathan, H.S., Tao, W.Q., 2014b. Pore-scale study of dissolution-induced changes in hydrologic properties of rocks with binary minerals. Water Resour. Res. 50, 5216–5234. https://doi.org/10.1002/2014WR015716.

Gray, F., Anabaraonye, B., Shah, S., Boek, E., Crawshaw, J., 2018. Chemical mechanisms of dissolution of calcite by HCl in porous media: simulations and experiment. Adv. Water Resour. 121, 369–387. https://doi.org/10.1016/j.advwatres.2018.09.007.

Hawez, H., Ahmed, Z., 2014. Enhanced oil recovery by CO_2 injection in carbonate reservoirs. WIT Trans. Ecol. Environ. 186, 547–558. https://doi.org/10.2495/ESUS140481.

Kang, Q., Zhang, D., Chen, S., 2003. Simulation of dissolution and precipitation in porous media. J. Geophys. Res. Solid Earth 108. https://doi.org/10.1029/2003JB002504.

Kumar, K., Van Noorden, T.L., Pop, I.S., 2011. Effective dispersion equations for reactive flows involving free boundaries at the microscale. Multisc. Model. Simul. 9 (1), 29–58. https://doi.org/10.1137/100804553.

Kumar, K., Wheeler, M.F., Thomas, W., 2013. Reactive flow and reaction-induced boundary movement in a thin channel. SIAM J. SCI. Comput. 35 (6), B1235–B1266. https://doi.org/10.1137/130913134.

Li, L., Steefel, C.I., Yang, L., 2008a. Scale dependence of mineral dissolution rates within single pores and fractures. Geochim. Cosmochim. Acta 72, 360–377. https://doi.org/10.1016/j.gca.2007.10.027.

Li, X., Huang, H., Meakin, P., 2008b. Level set simulation of coupled advection-diffusion and pore structure evolution due to mineral precipitation in porous media. Water Resour. Res. 44, 1–17. https://doi.org/10.1029/2007WR006742.

Li, Y.H., Gregory, S., 1974. Diffusion of ions in sea water and in deep-sea sediments. Geochim. Cosmochim. Acta 38 (5), 703–714. https://doi.org/10.1016/0016-7037(74)90145-8.

Liao, X., Gao, C., Wu, P., 2012. Assessment of CO_2 EOR and its geo-storage potential in mature oil reservoirs, changing oil field, China. Carbon Management Technology Conference. https://doi.org/10.7122/150031-MS.

Liu, C., Shang, J., Zachara, J.M., 2011. Multispecies diffusion models: a study of uranyl species diffusion. Water Resour. Res. 47 (12), 1–16. https://doi.org/10.1029/2011WR010575.

Mehmani, Y., Sun, T., Balhoff, M.T., Eichhubl, P., Bryant, S., 2012. Multiblock pore-scale modeling and upscaling of reactive transport: application to carbon sequestration. Transp. Porous Med. 95, 305–326. https://doi.org/10.1007/s11242-012-0044-7.

Nogues, J.P., Fitts, J.P., Celia, M.A., Peters, C.A., 2013. Permeability evolution due to dissolution and precipitation of carbonates using reactive transport modeling in pore networks. Water Resour. Res. 49, 6006–6021. https://doi.org/10.1002/wrcr.20486.

Pacala, S., Socolow, R., 2004. Stabilization wedges: solving the climate problem for the next 50 years with current technologies. Science 305, 968–972. https://doi.org/10.1126/science.1100103.

Parkhurst, D., Appelo, C., 2013. Description of input and examples for PHREEQC Version 3—A computer program for speciation, batch-reaction, one-dimensional transport, and inverse geochemical calculations U.S. Geol. Survey Water Resources Investigations Report https://pubs.usgs.gov/tm/06/a43/ .

Raoof, A., Nick, H.M., Wolterbeek, T.K.T., Spiers, C.J., 2012. Pore-scale modeling of reactive transport in wellbore cement under CO2 storage conditions. Int. J. Greenh. Gas Control 11, 67–77. https://doi.org/10.1016/j.ijggc.2012.09.012.

Raoof, A., Nick, H.M., Hassanizadeh, S.M., Spiers, C.J., 2013. PoreFlow: a complex pore-network model for simulation of reactive transport in variably saturated porous media. Comput. Geosci. 61, 160–174. https://doi.org/10.1016/j.cageo.2013.08.005.

Rathnaweera, T.D., Ranjith, P.G., Perera, M.S.A., 2016. Experimental investigation of geochemical and mineralogical effects of CO_2 sequestration on flow characteristics of reservoir rock in deep saline aquifers. Nat. Publ. Gr. https://doi.org/10.1038/srep19362.

Rochelle, C.A., Czernichowski-Lauriol, I., Milodowski, A.E., 2004. The impact of chemical reactions on CO_2 storage in geological formations: a brief review. Geol. Soc. London, Spec. Publ. 233, 87–106. https://doi.org/10.1144/GSL.SP.2004.233.01.07.

Shaw, J., Bachu, S., 2002. Screening, evaluation, and ranking of Oil reservoirs suitable for CO2-Flood EOR and carbon dioxide sequestration. J. Can. Pet. Technol. 41 (09). https://doi.org/10.2118/02-09-05.

Soulaine, C., Roman, S., Kovscek, A., Tchelepi, H.A., 2017. Mineral dissolution and wormholing from a pore-scale perspective. J. Fluid Mech. 827, 457–483. https://doi.org/10.1017/jfm.2017.499.

Starchenko, V., Marra, C.J., Ladd, A.J.C., 2016. Three-dimensional simulations of fracture dissolution. J. Geophys. Res. Solid Earth 121 (9), 6421–6444. https://doi.org/10.1002/2016JB013321.

Tansey, J., Balhoff, M.T., 2016. Pore network modeling of reactive transport and dissolution in porous media. Transp. Porous Media 113, 303–327. https://doi.org/10.1007/s11242-016-0695-x.

Van Noorden, T.L., 2009. Crystal precipitation and dissolution in a porous medium: effective equations and numerical experiments. Multiscale Model. Simul. 7 (3), 1220–1236. https://doi.org/10.1137/080722096.

Varloteaux, C., Békri, S., Adler, P.M., 2013a. Pore network modelling to determine the transport properties in presence of a reactive fluid: from pore to reservoir scale. Adv. Water Resour. 53, 87–100. https://doi.org/10.1016/j.advwatres.2012.10.004.

Varloteaux, C., Vu, M.T., Békri, S., Adler, P.M., 2013b. Reactive transport in porous media: pore-network model approach compared to pore-scale model. Phys. Rev. E 87, 023010. https://doi.org/10.1103/PhysRevE.87.023010.

Wolthers, M., Charlet, L., Van Cappellen, P., 2008. The surface chemistry of divalent metal carbonate minerals: a critical assessment of surface charge and potential data using the charge distribution multi-site ion complexation model. Am. J. Sci. 308, 905–941. https://doi.org/10.2475/08.2008.02.

Zeebe, R.E., Wolf-Gladrow, D.A., 2001. In: CO2 in Seawater : Equilibrium, Kinetics, Isotopes, 65. Elsevier, p. 346.